nature nanotechnology

LETTERS

https://doi.org/10.1038/s41565-020-0714-5

Check for updates

Bipolar-shell resurfacing for blue LEDs based on strongly confined perovskite quantum dots

Yitong Dong[1,9], Ya-Kun Wang[1,2,9], Fanglong Yuan[1,3,9], Andrew Johnston[1], Yuan Liu[1], Dongxin Ma[1], Min-Jae Choi[1], Bin Chen[1], Mahshid Chekini[4], Se-Woong Baek[1,7], Laxmi Kishore Sagar[1], James Fan[1], Yi Hou[1], Mingjian Wu[5], Seungjin Lee[1], Bin Sun[1], Sjoerd Hoogland[1], Rafael Quintero-Bermudez[1], Hinako Ebe[1], Petar Todorovic[1], Filip Dinic[6], Peicheng Li[3], Hao Ting Kung[3], Makhsud I. Saidaminov[1,8], Eugenia Kumacheva[4], Erdmann Spiecker[5], Liang-Sheng Liao[2], Oleksandr Voznyy[6], Zheng-Hong Lu[3]✉ and Edward H. Sargent[1]✉

Colloidal quantum dot (QD) solids are emerging semiconductors that have been actively explored in fundamental studies of charge transport[1] and for applications in optoelectronics[2]. Forming high-quality QD solids—necessary for device fabrication—requires substitution of the long organic ligands used for synthesis with short ligands that provide increased QD coupling and improved charge transport[3]. However, in perovskite QDs, the polar solvents used to carry out the ligand exchange decompose the highly ionic perovskites[4]. Here we report perovskite QD resurfacing to achieve a bipolar shell consisting of an inner anion shell, and an outer shell comprised of cations and polar solvent molecules. The outer shell is electrostatically adsorbed to the negatively charged inner shell. This approach produces strongly confined perovskite QD solids that feature improved carrier mobility ($\geq$0.01 $cm^2 V^{-1} s^{-1}$) and reduced trap density relative to previously reported low-dimensional perovskites. Blue-emitting QD films exhibit photoluminescence quantum yields exceeding 90%. By exploiting the improved mobility, we have been able to fabricate $CsPbBr_3$ QD-based efficient blue and green light-emitting diodes. Blue devices with reduced trap density have an external quantum efficiency of 12.3%; the green devices achieve an external quantum efficiency of 22%.

Quantum confinement increases the binding energy of excitons in perovskites, positioning these materials for use in next-generation light-emitting diodes (LEDs)[5–7]. In perovskite quantum dots (QDs), quantum confinement offers an additional method, beyond anion substitution[8,9], to tune the emission wavelength and avoid halide segregation in QD LEDs.

In traditional chalcogenide QD optoelectronic devices, solution-phase ligand exchange results in close-packed QD solid films exhibiting high carrier mobility (~0.03 $cm^2 V^{-1} s^{-1}$)[10]. Before film formation occurs, QDs are sterically stabilized with long-chain ligands that are exchanged with short charged molecules, and the QDs are further stabilized by the counterions that diffuse to the double electric layer from the bulk polar solvent[11].

However, managing colloidal stability and short-ligand passivation while retaining confinement is a challenge specific to perovskite QDs. Perovskite QD surfaces are terminated with LH^+X^- ion pairs[12], where LH^+ represents the hydrated organic ligand and X^- is a combination of long-chain carboxylate ligands and halide ions. The non-covalent ligand–surface bond in perovskites results in dynamic ligand binding[13]. The QD surface ions can be stripped off, along with the organic ligands, upon ligand exchange ($LH^+ + Br^- \rightleftharpoons L + HBr$), destabilizing QD colloids and reducing the photoluminescence quantum yield (PLQY)[14].

We pursued a bipolar-shell-resurfacing approach to stabilize perovskite QDs electrostatically with the aid of atomic ligands. Monodispersed $CsPbBr_3$ perovskite QDs with strong quantum confinement were synthesized according to a previously reported method[15]. QDs of two diameters (4 and 7 nm) were used to investigate the general nature of the ligand exchange. Figure 1a–d depicts the $CsPbBr_3$ QD resurfacing processes and the electrokinetic potential (ζ potential) of each corresponding step (Fig. 1a–d) compared with traditional ligand exchange (Fig. 1f). The as-synthesized QDs, sterically stabilized using long-chain organic ligands (oleylamine and oleic acid) in toluene, have negligible ζ potential (Fig. 1a). These ligands were stripped off during QD reprecipitation following the addition of a non-solvent (methyl acetate) to a toluene solution of QDs[16]. Due to dynamic organic ligand binding to the QD surface, surface bromide anions were lost during the precipitation process, and the QD surface gained a weak charge, exhibiting a small positive ζ potential (Fig. 1b).

To address the bromide deficiency in the QDs, a saturated solution of dimethylformamide (DMF)/toluene containing isopropylammonium bromide (IPABr) was added to the QD solution after multiple reprecipitations. The IPABr adhered to the QD, forming a Br^--rich surface, a finding confirmed by X-ray photoemission

[1]Department of Electrical and Computer Engineering, University of Toronto, Toronto, Ontario, Canada. [2]Institute of Functional Nano and Soft Materials (FUNSOM), Jiangsu Key Laboratory for Carbon-Based Functional Materials & Devices, Soochow University, Suzhou, PR China. [3]Department of Materials Science and Engineering, University of Toronto, Toronto, Ontario, Canada. [4]Department of Chemistry, University of Toronto, Toronto, Ontario, Canada. [5]Centre for Nanoanalysis and Electron Microscopy (CENEM) and Institute of Micro- and Nanostructure Research, Friedrich-Alexander-Universität Erlangen-Nürnberg, Erlangen, Germany. [6]Department of Physical and Environmental Sciences, University of Toronto Scarborough, Scarborough, Ontario, Canada. [7]Present address: Department of Chemical and Biological Engineering, Korea University, Seoul, Korea. [8]Present address: Department of Chemistry and Electrical and Computer Engineering, Centre for Advanced Materials and Related Technologies (CAMTEC), University of Victoria, Victoria, British Columbia, Canada. [9]These authors contributed equally: Yitong Dong, Ya-Kun Wang, Fanglong Yuan. ✉e-mail: zhenghong.lu@utoronto.ca; ted.sargent@utoronto.ca

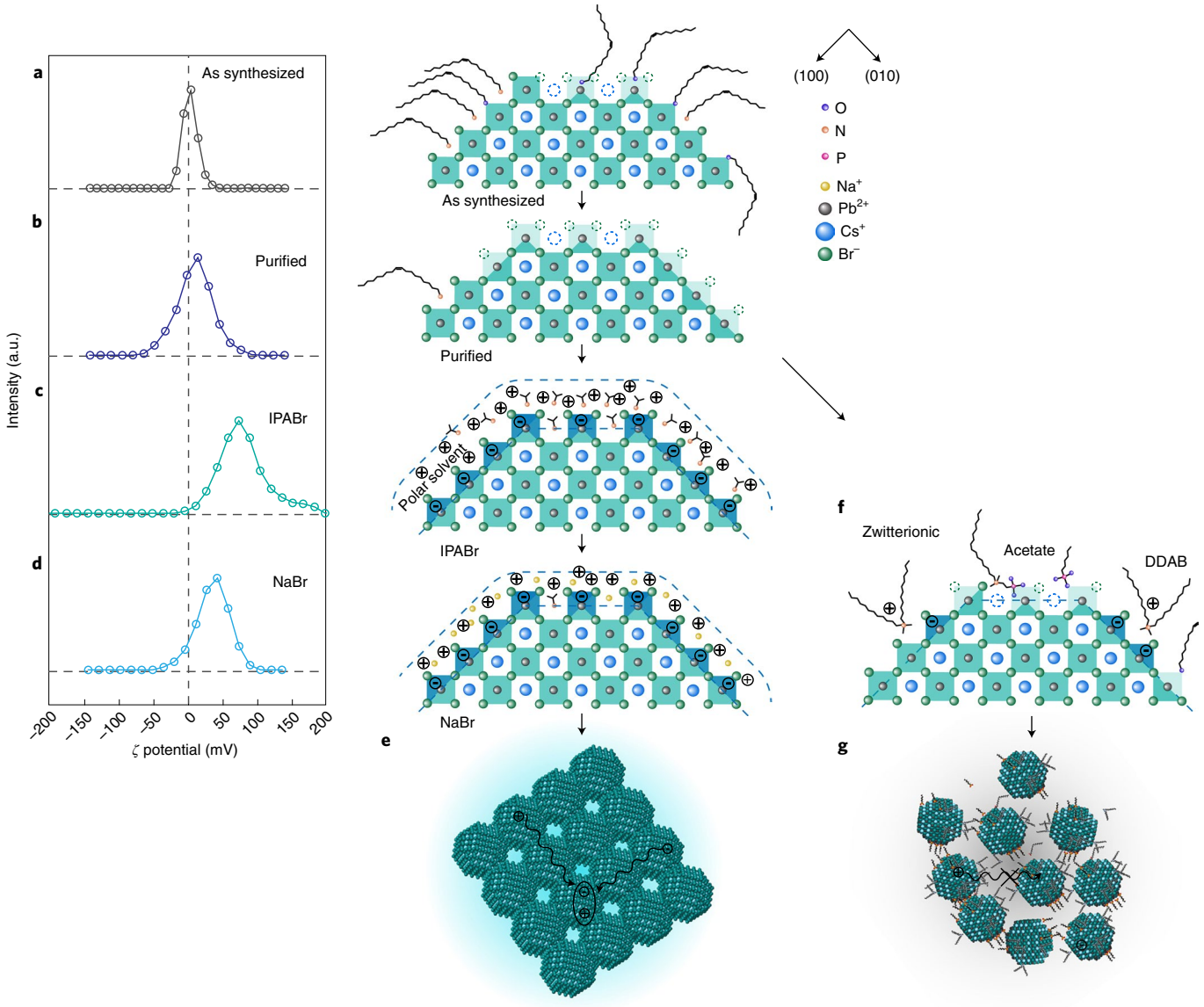

Fig. 1 | Bipolar-shell resurfacing of perovskite QDs. a–d, ζ potentials (left) and schematics (right) of QD surfaces. **a**, The surface of as-synthesized perovskite QDs capped using long organic ligands and showing near-zero ζ potential. The QD surface is neutral and sterically stabilized. QDs became polyhedral after purification. X-ray diffraction shows the appearance of (110) and (111) facets (Supplementary Fig. 1a). Arrows on the right indicate the direction of the (100) and (010) facets. **b**, Purified QDs with surface defects (undercoordinated Pb^{2+}) and exhibiting slight positive charges. The QDs gained weak positive charge and a low, positive ζ potential. **c**, QD resurfacing with isopropylammonium bromide. Surface vacancies were passivated and a bipolar solvent shell formed around the surface of the QDs. **d**, QD surface following cation substitution using Na^+. The bipolar-shell-protected QDs in **c** and **d** show strong positive ζ potential. The reduction in ζ potential after NaBr treatment implies that the cation concentration in the outer QD shell was decreased after NaBr/DMF exchange, a finding that we ascribe to the limited solubility of NaBr in DMF.**e**, Solids formed with resurfaced perovskite QDs with high PLQYs. A short inter-QD distance enabled more efficient charge transport among QDs. **f**, QD surface passivated with traditional long-chain organic ligands. Steric effects arise from the use of bulky ligands because these cannot be densely packed near the QD surface. **g**, Film cast from perovskite QDs with long-chain organic ligands, which result in larger interdot spacing.

spectroscopy (XPS) elemental analysis (Br/Pb = 3.4/1, Supplementary Fig. 2). Simultaneously, the counterions (for example, isopropylammonium cations) solvated by polar DMF surrounded the QDs, forming an outer shell (Fig. 1c). As a result of the positively charged, cation-enriched polar solvent outer shell, the QDs exhibited a high positive ζ potential of ~90 mV (Fig. 1c). The two-dimensional nuclear Overhauser enhancement spectroscopy (2D NOESY) ^{1}H NMR spectra of QDs (Supplementary Fig. 3b) showed a negative off-diagonal signal, in agreement with the presence of polar solvent protons (DMF and acetates), as well as ammonium cations, on the QD surface. In contrast, the ζ potential of control didodecyldimethylammonium bromide (DDAB)-capped QDs without the bilayer structure in toluene (Fig. 1f), after the same precipitation procedure[17], is ~−30 mV (Supplementary Fig. 1b).

Next, we replaced the ammonium countercations in the outer shell via an additional exchange step that involved a NaBr-saturated DMF solution. The remaining organic ligands were removed from the surface during the NaBr/DMF treatment (Fig. 1e): 1D and 2D NOESY ^{1}H NMR spectra showed no vinyl proton signals at 5.5 ppm and negligible C–H protons in off-diagonal regions

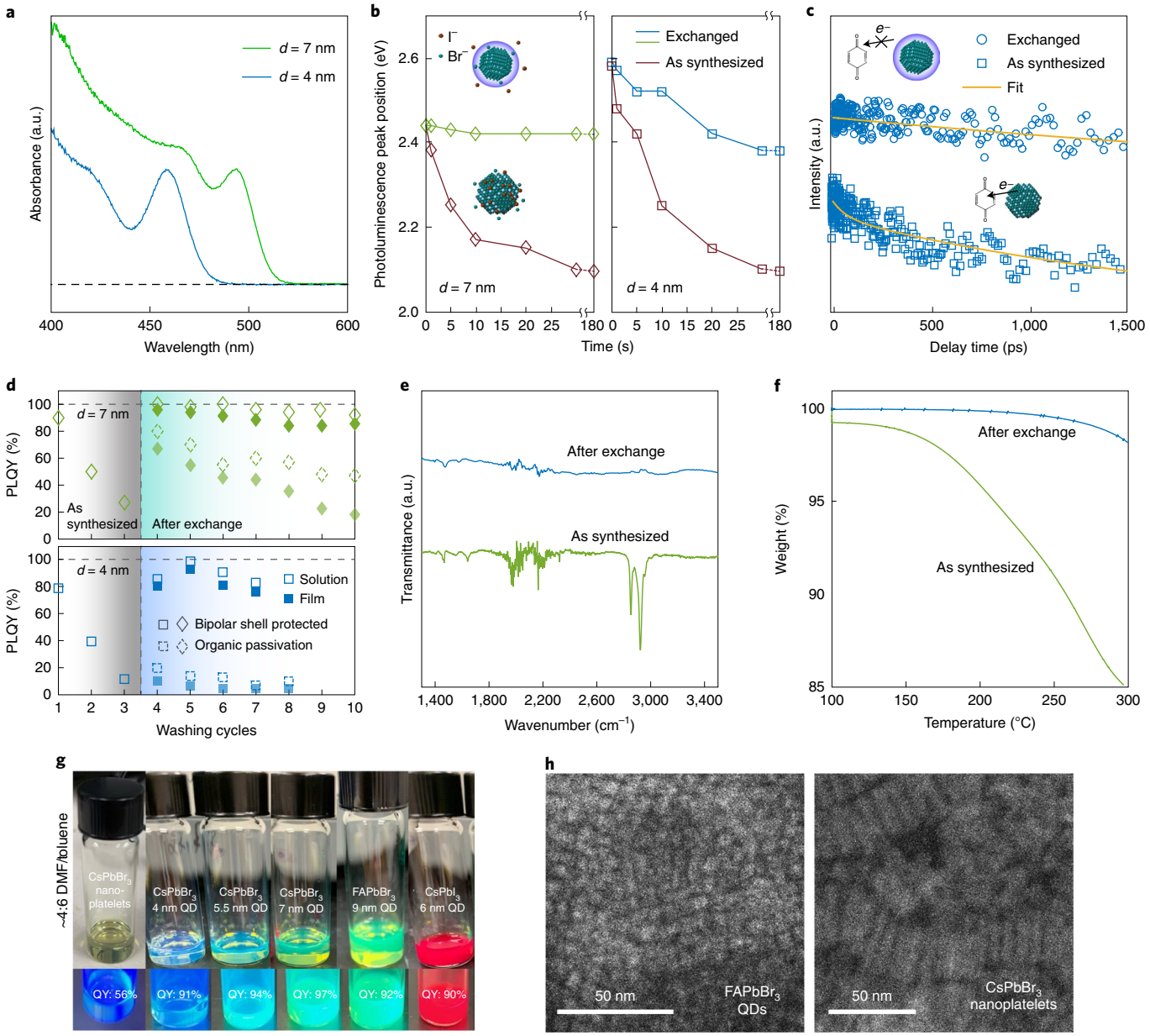

Fig. 2 | Chemistry and photophysics of bipolar-shell-stabilized $CsPbBr_3$ perovskite QDs. a, Absorption spectra of QDs of two different diameters (*d*). **b**, Anion exchange rate monitored from the photoluminescence peak shift at different reaction times. Exchanged QDs show that the bipolar shell suppressed anion exchange (schematic in the insets) for ≥180 s, with a photoluminescence peak shift of <50 meV for 7 nm QDs and <200 meV for 4 nm QDs. **c**, Transient absorption bleach recovery dynamics monitored at 470 nm for original QDs and bipolar-shell-stabilized QDs in the presence of the electronic quencher benzoquinone. The bipolar shell prevents benzoquinone molecules from being adsorbed on the QD surface (schematic in the insets). **d**, PLQYs of QDs and QD solid films made from DDAB-treated perovskite QDs and bipolar-shell-stabilized QDs of two different diameters (empty symbols represent solution and filled symbols represent solid film). The grey area represents washing iterations without ligand exchange process and the green and blue areas represent iterations using bipolar exchanges or DDAB ligand exchanges, respectively. Films cast from the optimally exchanged QDs maintained a high PLQY (>70% for 4 nm QDs) under low excitation density (<1 mW cm^{-2}, details in Supplementary Fig. 6) even following purification. **e**, FTIR spectra of QD films cast with as-synthesized QDs and bipolar-shell-stabilized QDs. **f**, TGA of perovskite QDs with and without bipolar-shell stabilization. **g**, Bipolar resurfaced perovskite nanocrystals of various sizes, shapes and compositions suspended in DMF/toluene mixture. **h**, TEM images of close-packed bipolar resurfaced formamidinium lead bromide ($FAPbBr_3$) QDs and $CsPbBr_3$ nanoplatelets. The interparticle distances are reduced to <0.5 nm, indicating exchanged ligand.

(Supplementary Fig. 3a,c). XPS analysis showed no detectable signal in the N1*s* region, indicating that the ammonium group was replaced with Na^+ (Supplementary Fig. 2d). The positive ζ potential observed (~40 meV) indicates that the bipolar-shell structure remained intact (Fig. 1d). The QD solution exhibited excellent stability: the PLQY remained invariant over a six-month period of benchtop storage.

The bipolar resurfacing approach is suitable for perovskite QDs with a range of bandgaps, shapes and compositions. We achieved successful exchanges and redispersions in each case (Fig. 2g,h and Supplementary Figs. 4 and 5).

To explore further the bipolar-shell model, we measured the anion exchange rate during the exchange process. The anion exchange reaction rate is fast (<1 s) in colloidal nanoparticles[8], but is

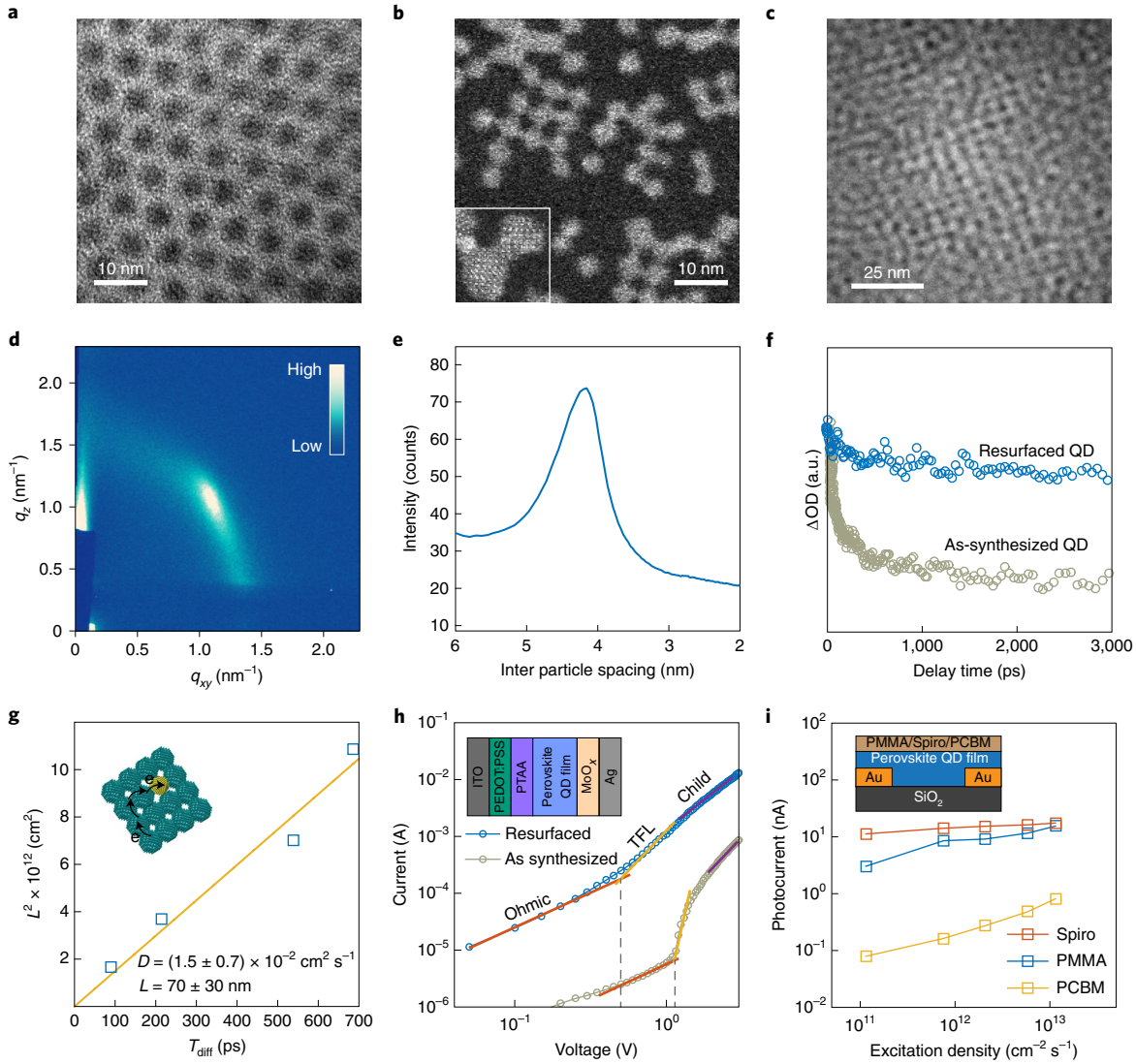

Fig. 3 | Properties of $CsPbBr_3$ perovskite QD solid films cast from bipolar-shell-resurfaced QD inks. a, TEM image of purified perovskite QDs ~4 nm in diameter. Interparticle spacing is >2 nm, and this spacing is dominated by the length of the original organic ligands. **b**, Low-dose STEM Z-contrast image of electronically stabilized perovskite QDs. The QDs self-assemble and produce an atomic-scale interparticle distance. The inset shows two adjacent QDs. Edge-to-edge assembly alignment can be seen. **c**, Large-scale TEM image of QD solids formed by spin-coating QD inks on the TEM grid. **d**, Two-dimensional GISAXS pattern of the perovskite QD solid plotted in reciprocal space (*q*-space). The dark colour represents lower intensity and the bright colour represents higher intensity. **e**, Azimuthally integrated GISAXS intensities of perovskite QD solids. The sharp peak shows the average distribution of the interparticle distance of 4.2 nm. **f**, Comparison of transient absorption bleach recovery dynamics of QD films cast from bipolar-shell-resurfaced QDs and as-synthesized QDs monitored at the band edge. **g**, Diffusion coefficient of excitons (*D*) in perovskite QD solids measured via transient absorption spectroscopy by adding PbS QDs of the same size as the perovskite QDs as quenchers (the solids are depicted in the inset, the exciton diffusion lifetime (T_{diff}) is obtained by fitting the TA trace using a monoexponential model (see Supplementary Fig. 9 and Supplementary Table 2)). **h**, Current density versus voltage curves for hole-only devices under dark conditions. Inset shows the device structure (ITO, indium tin oxide; PEDOT:PSS, poly(3,4-ethylenedioxythiophene) polystyrene sulfonate; PTAA, poly(triaryl)amine). SCLC fits (solid lines) reveal the hole mobility and the trap-filling limit voltage (V_{TFL}), showing reduced trap densities of QD solids made using resurfaced dots. The inset shows the device structure. **i**, Photocurrent as a function of the intensity of a 405 nm excitation laser for photoresistors fabricated using perovskite QD solids. The inset shows the device structure. The QD solid is covered with a hole-accepting *N*2,*N*2,*N*2′,*N*2′,*N*7,*N*7,*N*7′,*N*7′-octakis(4-methoxyphenyl)-9,9′-spirobi[fluorene]-2,2′,7,7′-tetraamine layer (Spiro), an electron-accepting [6,6]-phenyl-C61-butyric acid methyl ester layer (PCBM), or a poly(methyl methacrylate) layer (PMMA) layer for electron-only, hole-only and exciton studies, respectively. The high electron-only photocurrent and relatively lower hole-only current indicate that the main trapping sites in the QD solid are hole traps.

expected to slow in the presence of a solvated shell around the QDs. Indeed, the bipolar-shell-protected QDs exhibited a small photoluminescence redshift over a long period (Fig. 2b). In contrast, the as-synthesized QDs capped with long organic ligands underwent a fast (<5 s) iodide anion exchange and showed a large photoluminescence shift (Fig. 2b) over the same reaction time. To explore further the effect of the bipolar shell, an electron quencher (benzoquinone) was added to the QD solution to extract band-edge electrons from the QD surface[18]. We used transient absorption dynamics to monitor the carrier population at the band edge and found an absence of fast band-edge electron transfer in the bipolar-shell-stabilized QDs (Fig. 2c); in contrast, the as-synthesized QDs (Fig. 2c) showed

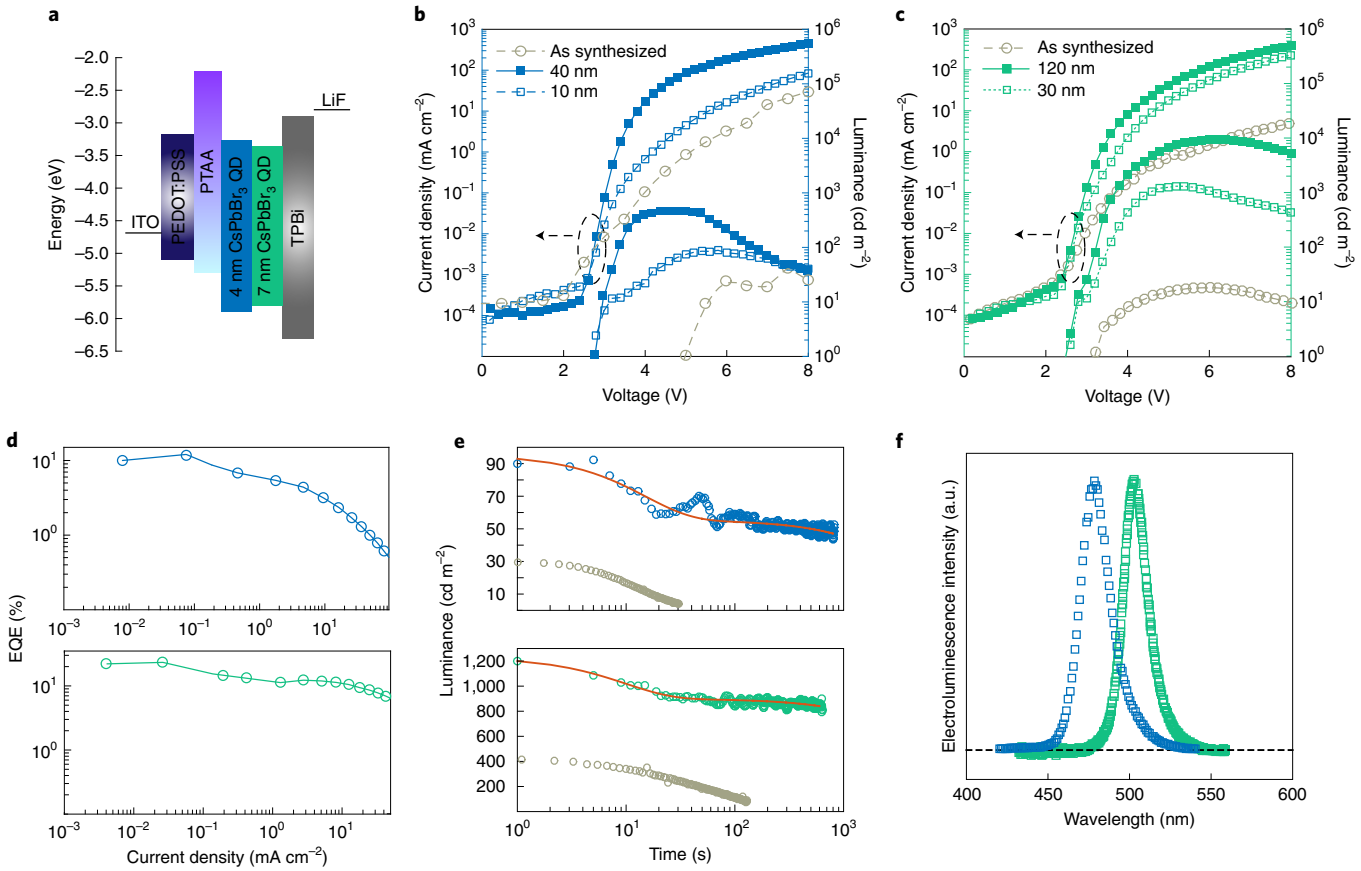

Fig. 4 | Blue and green LEDs based on perovskite QD solids. a, Schematic of LEDs fabricated using perovskite QD solids. TPBi, 2,2′,2″-(1,3,5-benzinetriyl)-tris(1-phenyl-1-*H*-benzimidazole). **b**,**c**, Current density versus voltage and luminance versus current density curves of blue LEDs (**b**) and green LEDs (**c**) with different QD solid thickness. **d**, EQE of blue and green LED devices. **e**, Operating stability curve and fit (solid lines) of blue and green LEDs at luminances of 90 cd m^{-2} (top) and 1,200 cd m^{-2} (bottom). **f**, Electroluminescence spectra of blue (4 nm QDs) and green (7 nm QDs) LEDs.

a rapid bleach decay in the first ~100 ps, indicating that the bipolar shell protected these QDs from benzoquinone adsorption.

The electronic structure near the band edge of $CsPbX_3$ arises from the *s*,*p* antibonding states of Pb and halide atoms[19,20]. Ab initio calculations have previously shown that electrons become localized in the mid-gap states created by halide vacancies[16]. As the degree of quantum confinement increases, so too does the relative energetic depth of the traps, accentuating the impact on charge transport and luminescence. After the bipolar-shell exchange, the halide vacancies are thoroughly passivated by the tight bromide inner shell. Therefore, QDs exhibited near-unity PLQYs (Fig. 2d). In comparison, 7 nm QDs after DDAB treatment showed 20% lower PLQYs, and DDAB fails to passivate 4 nm QDs: no noticeable PLQY increase is observed following treatment (Fig. 2d). In addition, the outer cation-enriched polar solvent shell suppressed dynamic ligand–ion pair equilibrium and, as a result, the PLQYs of QD colloids remained high even after 5–7 iterations of purification (Fig. 2d). In comparison, purified DDAB-capped QDs lost ~50% of their PLQYs during film casting (Fig. 2d). It is worth noting that any loss of PLQY observed after purification can be readily recovered with the addition of a small amount of polar solvent containing bromide anions.

Fourier transform infrared (FTIR) spectra of films formed from exchanged QDs were virtually featureless, whereas the original QD films showed clear C–H and N–H bends in the 2,800–3,000 cm^{-1} region (Fig. 2e). ^{1}H NMR spectra also revealed that oleate ligands were largely removed from the QD surface: the 4–6 ppm oleate proton intensities were substantially decreased (Supplementary Fig. 3). In addition, thermogravimetric analysis (TGA) of exchanged QDs showed only ~2% weight loss up to 300 °C, whereas QDs capped with long organic ligands showed 15% weight loss (Fig. 2f).

Transmission electron microscopy (TEM) images of spin-cast QD film show the self-assembly of the QDs (Fig. 3b,c and Supplementary Fig. 7a–c). The inter-QD distance (~4.2 nm, Fig. 3b) in TEM is smaller than that of QDs with normal organic ligands (6–7 nm) (Fig. 3a). The observed grazing-incidence small-angle X-ray scattering (GISAXS) diffraction pattern (Fig. 3d) indicates orientational ordering of the monodispersed QDs. Azimuthal integration of the diffraction pattern showed a sharp peak with an inter-QD distance of 4.2 nm (Fig. 3e). This is in good agreement with the inter-QD distance obtained by TEM. Although the QD solid films formed using 7-nm-diameter particles were disordered, the interparticle distance remained small (Supplementary Fig. 7d,e). The small interparticle distance (<2 Å) and strong quantum confinement resulted in improved interparticle coupling, supported by the ~10 nm photoluminescence peak redshift observed for the QD solid films compared with the photoluminescence peak position of the QDs in solution (Supplementary Fig. 8).

As seen in Fig. 3f, transient absorption bleach recovery dynamics at the band edge shows a 4 ns recovery time for resurfaced QD films, whereas films cast from as-synthesized QDs showed a rapid bleach recovery signal (<500 ps) due to trap formation induced by ligand loss during film casting. This agrees with the high PLQY values measured in films in Fig. 2d.

We then evaluated the carrier mobility and trap density of QD solids using transient absorption spectroscopy, space-charge-limited

current (SCLC) and photocurrent measurements (Supplementary Fig. 9). By introducing different concentrations of PbS QDs of the same size as $CsPbBr_3$ QDs (Methods)[21], we estimated the exciton diffusion length to be ~70 ± 30 nm (Fig. 3g), which is comparable to that in QD solids formed in chalcogenide QDs by atomic ligand exchange[22].

We also built electron-only and hole-only devices for electrical transport measurements (Methods). From the Child region (Fig. 3h and Supplementary Fig. 9c), based on analysis using the Mott–Gurney equation (details in Supplementary Information), we obtain electrical transports of $\mu_e = 0.02\,cm^2\,V^{-1}\,s^{-1}$ and $\mu_h = 0.01\,cm^2\,V^{-1}\,s^{-1}$ (where the subscripts 'e' and 'h' indicate electrons and holes, respectively). These values are higher than in previously reported perovskite QD films[7] and 2D perovskite thin films of similar bandgap ($\leq 1 \times 10^{-4}\,cm^2\,V^{-1}\,s^{-1}$)[23].

Using SCLC, we also estimated the trap state densities in QD solids from:

$$n_{t(e/h)} = 2\varepsilon\varepsilon_0 V_{TFL(e/h)}/(ed^2) \quad (1)$$

where n_t is the trap state density, V_{TFL} is the trap-filled limit voltage, d is the distance between the electrodes, e is the elementary charge and ε_0 and ε are the vacuum permittivity and relative permittivity, respectively. The trap state densities are $n_{te} = 3 \times 10^{14}\,cm^{-3}$ and $n_{th} = 1 \times 10^{15}\,cm^{-3}$, which are an order of magnitude lower than in QD films of as-synthesized dots (Supplementary Table 4).

We sought an additional, independent probe of electron and hole transport behaviour through photocurrent studies[24] (Fig. 3i and Supplementary Fig. 10, details in Supplementary Information). The electron-only photocurrent is approximately an order of magnitude higher than the hole-only photocurrent (Supplementary Fig. 11), consistent with the anticipation of reduced surface ligand loss during film casting because unpassivated Pb^{2+} is usually considered to be an electron trap. We also conducted photovoltaic external quantum efficiency measurements using sub-bandgap excitation, and observed a reduced concentration and depth of band-tail states in bipolar resurfaced QD films (Supplementary Fig. 9d).

Blue perovskite LEDs that showcased promising efficiencies have recently been reported[6,25]; however, when the requirements for primary blue emission colour (≤480 nm, defined by chromaticity with CIE y-coordinate value <~0.13) and spectral stability are added, the external quantum efficiencies (EQEs) in blue have remained ≤6%. Encouraged by the improved mobility and greatly reduced trap densities in the bipolar resurfaced dots, we fabricated LEDs using the QD solids. Our blue devices exhibited a narrow emission linewidth of ≤20 nm, compared with >25 mm reported for LEDs (Fig. 4f)[6,26]. The best of these blue devices showed an EQE value of 12.3% (Fig. 4d and Supplementary Fig. 12). Compared with blue perovskite LEDs and control devices that employ purified as-synthesized QDs following a reported method[27], LEDs using resurfaced QDs show lower turn-on voltages (only ~0.1 eV above the bandgap, Fig. 4b,c).

We evaluated the impact of the mobility on operating voltage and current density in LEDs by simulating the current density versus voltage characteristics[28,29] utilizing the mobility values measured experimentally (details in Supplementary Information). They reveal that the increased carrier mobility facilitates the charge injection needed to reduce the turn-on voltage (Supplementary Figs. 13 and 14).

To take advantage of the increased mobility, we optimized the QD solid thickness. We estimated the recombination zone width (details in Supplementary Information). Improved carrier mobility expands the recombination zone, and an active layer that is thinner than the recombination zone width will limit the carrier recombination rate because the recombination zone will extend outside of the lowest-bandgap emission region.

The recombination zone width is estimated to be ~70 nm for blue QD solids and ~130 nm for green QD solids (details in Supplementary Information). The luminance of both blue and green devices with QD film thickness matching the recombination zone width increased by about fivefold compared with that of devices with about fourfold thinner active layers (Fig. 4b,c and Supplementary Fig. 15). Additionally, a thicker, more continuous QD film increases the volume of QDs that remain unaffected by the contacting charge transport materials. This will, in turn, mitigate the possible unfavourable injection condition within thin QD films. We investigate further the dependence of device current density on QD layer thickness using simulation (Supplementary Figs. 16 and 17).

LEDs from resurfaced perovskite QD solids showed no measurable shift in electroluminescence spectral peak over time under applied bias (Supplementary Fig. 18). The best blue perovskite LEDs have thus far exhibited limited operational stability (<10 min T_{50}), a finding attributed to ion migration with the aid of surface traps[23]. Devices made using bipolar-shell QDs showed enhanced stability: a 60 min half lifetime (T_{50}) at 1,200 cd m^{-2} for the green LEDs and a 20 min T_{50} at 90 cd m^{-2} for blue LEDs (Fig. 4e), ~5-fold longer than the best reported blue perovskite LEDs without electroluminescence spectra shift[6].

Given that $CsPbX_3$ are known to have limited thermal conductivity[30], we also investigated devices in a pulsed operation mode to mitigate heating (Methods). We observed that the electroluminescence intensity decreased with longer pulse duration (Supplementary Fig. 19). Compared with continuous-wave mode, the electroluminescence intensity was improved when the device was driven using ~1 ms electric pulses (Supplementary Fig. 18). The improvement in intensity is particularly noticeable at large biases where roll-off begins (~5 V). The EQE of each class of device was also higher at a greater current density under pulsed mode (Supplementary Fig. 20).

The LED operating stability curve was fitted using two-component exponential decay (Fig. 4e). The time-dependent electroluminescence intensity curve starts with a fast decay (<20 s, attributed to thermal decay). After thermal equilibrium was achieved in the first 15–20 s, the electroluminescence intensity decay slowed by nearly two orders of magnitude. The fast decay of the electroluminescence intensity is suppressed in the short-pulse mode (Supplementary Fig. 18).

In conclusion, we employed a solution-based ligand exchange to stabilize perovskite QD colloids with bipolar shells. The QD inks resulted in close-packed QD solid films with near-unity PLQYs and high charge-carrier mobilities. Additionally, efficient LEDs were fabricated using the differently sized QDs, and both the green and blue LEDs exhibited enhanced operational stability. The work further confirms that suitably managed perovskite nanocrystals show promise for use in next-generation LEDs.

Online content

Any methods, additional references, Nature Research reporting summaries, source data, extended data, supplementary information, acknowledgements, peer review information; details of author contributions and competing interests; and statements of data and code availability are available at https://doi.org/10.1038/s41565-020-0714-5.

Received: 19 December 2019; Accepted: 11 May 2020;
Published online: 06 July 2020

References

1. Kagan, C. R. & Murray, C. B. Charge transport in strongly coupled quantum dot solids. *Nat. Nanotechnol.* **10**, 1013–1026 (2015).
2. A decade of perovskite photovoltaics. *Nat. Energy* **4**, 1 (2019).
3. Kagan, C. R., Lifshitz, E., Sargent, E. H. & Talapin, D. V. Building devices from colloidal quantum dots. *Science* **353**, 885–892 (2016).
4. Kovalenko, M. V., Protesescu, L. & Bodnarchuk, M. I. Properties and potential optoelectronic applications of lead halide perovskite nanocrystals. *Science* **358**, 745–750 (2017).
5. Yuan, M. et al. Perovskite energy funnels for efficient light-emitting diodes. *Nat. Nanotechnol.* **11**, 872–877 (2016).

6. Liu, Y. et al. Efficient blue light-emitting diodes based on quantum-confined bromide perovskite nanostructures. *Nat. Photon.* **13**, 760–764 (2019).
7. Chiba, T. et al. Anion-exchange red perovskite quantum dots with ammonium iodine salts for highly efficient light-emitting devices. *Nat. Photon.* **12**, 681–687 (2018).
8. Nedelcu, G. et al. Fast anion-exchange in highly luminescent nanocrystals of cesium lead halide perovskites ($CsPbX_3$, X = Cl, Br, I). *Nano Lett.* **15**, 5635–5640 (2015).
9. Akkerman, Q. A. et al. Tuning the optical properties of cesium lead halide perovskite nanocrystals by anion exchange reactions. *J. Am. Chem. Soc.* **137**, 10276–10281 (2015).
10. Kovalenko, M. V., Scheele, M. & Talapin, D. V. Colloidal nanocrystals with molecular metal chalcogenide surface ligands. *Science* **324**, 1417–1420 (2009).
11. Boles, M. A., Ling, D., Hyeon, T. & Talapin, D. V. The surface science of nanocrystals. *Nat. Mater.* **15**, 141–153 (2016).
12. Bodnarchuk, M. I. et al. Rationalizing and controlling the surface structure and electronic passivation of cesium lead halide nanocrystals. *ACS Energy Lett.* **4**, 63–74 (2019).
13. De Roo, J. et al. Highly dynamic ligand binding and light absorption coefficient of cesium lead bromide perovskite nanocrystals. *ACS Nano.* **10**, 2071–2081 (2016).
14. Krieg, F. et al. Colloidal $CsPbX_3$ (X = Cl, Br, I) nanocrystals 2.0: zwitterionic capping ligands for improved durability and stability. *ACS Energy Lett.* **3**, 641–646 (2018).
15. Dong, Y. et al. Precise control of quantum confinement in cesium lead halide perovskite quantum dots via thermodynamic equilibrium. *Nano Lett.* **18**, 3716–3722 (2018).
16. Nenon, D. P. et al. Design principles for trap-free $CsPbX_3$ nanocrystals: enumerating and eliminating surface halide vacancies with softer Lewis bases. *J. Am. Chem. Soc.* **140**, 17760–17772 (2018).
17. Pan, J. et al. Highly efficient perovskite-quantum-dot light-emitting diodes by surface engineering. *Adv. Mater.* **28**, 8718–8725 (2016).
18. Wu, K. et al. Ultrafast interfacial electron and hole transfer from $CsPbBr_3$ perovskite quantum dots. *J. Am. Chem. Soc.* **137**, 12792–12795 (2015).
19. Becker, M. A. et al. Bright triplet excitons in caesium lead halide perovskites. *Nature* **553**, 189–193 (2018).
20. Tao, S. et al. Absolute energy level positions in tin- and lead-based halide perovskites. *Nat. Commun.* **10**, 2560 (2019).
21. Gong, X. et al. Contactless measurements of photocarrier transport properties in perovskite single crystals. *Nat. Commun.* **10**, 1591 (2019).
22. Whitham, K. et al. Charge transport and localization in atomically coherent quantum dot solids. *Nat. Mater.* **15**, 557–563 (2016).
23. Li, Z. et al. Modulation of recombination zone position for quasi-two-dimensional blue perovskite light-emitting diodes with efficiency exceeding 5%. *Nat. Commun.* **10**, 1027 (2019).
24. Leijtens, T. et al. Carrier trapping and recombination: the role of defect physics in enhancing the open circuit voltage of metal halide perovskite solar cells. *Energy Environ. Sci.* **9**, 3472–3481 (2016).
25. Hou, S., Gangishetty, M. K., Quan, Q. & Congreve, D. N. Efficient blue and white perovskite light-emitting diodes via manganese doping. *Joule* **2**, 2421–2433 (2018).
26. Xing, J. et al. Color-stable highly luminescent sky-blue perovskite light-emitting diodes. *Nat. Commun.* **9**, 3541 (2018).
27. Chiba, T. et al. High-efficiency perovskite quantum-dot light-emitting devices by effective washing process and interfacial energy level alignment. *ACS Appl. Mater. Interfaces* **9**, 18054–18060 (2017).
28. Gong, X. et al. Highly efficient quantum dot near-infrared light-emitting diodes. *Nat. Photon.* **10**, 253–257 (2016).
29. Shen, H. et al. Visible quantum dot light-emitting diodes with simultaneous high brightness and efficiency. *Nat. Photon.* **13**, 192–197 (2019).
30. Lee, W. et al. Ultralow thermal conductivity in all-inorganic halide perovskites. *Proc. Natl Acad. Sci. USA* **114**, 8693–8697 (2017).

Methods

$CsPbBr_3$ QD synthesis and purification. $CsPbBr_3$ QDs were synthesized and purified by a previously reported method[15]. In brief, 300 mg of Cs_2CO_3, 1.2 ml of oleic acid and 3.2 ml of 1-octadecene were dried in a three-necked round-bottom flask at room temperature for 15 min. In another flask, 700 mg of $PbBr_2$ and 1,400 mg of $ZnBr_2$ were mixed with 14 ml of oleylamine/oleic acid mixture and 40 ml of 1-octadecene, followed by vacuum drying at 150 °C for 10 min. The lead halide precursors were kept under a nitrogen atmosphere at the reaction temperatures (80 °C for 4 nm QDs and 210 °C for 7 nm QDs) until all solids were dissolved. Then 3.0–3.2 ml of Cs precursor solution was swiftly injected into the flask containing the lead halide precursor. After a chosen reaction time (3 min for 4 nm QDs and 10 s for 7 nm QDs), the solution was cooled using an ice water bath. The solution was centrifuged at 7,800 r.p.m. to remove unreacted precursors. For 7 nm QDs, the precipitant was collected because the particles are heavier, whereas for 4 nm QDs the supernatant was collected. The purification process used depended on the diameter of QDs. For 7 nm QDs, the precipitants were dispersed in 7 ml of toluene followed by the addition of 20 ml of methyl acetate. The mixture was centrifuged at 7,800 r.p.m. to collect the precipitants. For 4 nm QDs, the supernatant was allowed to stand on the benchtop for 24 h until white precipitants appeared. After the removal of any undissolved solids, ~20 ml of acetone was added and the mixture was vortexed until turbid. Then the mixture was centrifuged at 7,800 r.p.m. to collect the precipitant. Additional acetone is required in cases in which the mixture was clear following vortexing.

Ligand exchange and bipolar-shell-resurfaced QD ink preparation. QDs suspended in toluene were purified up to three times by precipitating using methyl acetate. Briefly, ~30 ml of methyl acetate was added into ~7 ml of QD solution in toluene. The mixture was vortexed for 1 min and then centrifuged at 7,800 r.p.m. for 3 min. The precipitants were collected and resuspended in ~5 ml of toluene. This procedure was repeated once or twice. The final QD precipitants were suspended into ~1.5 ml of toluene for ligand exchange.

For ligand exchange, 250 mg of IPABr was dissolved into 0.5 ml of DMF and diluted with 0.5 ml of toluene. Saturated NaBr DMF solution was prepared by sonicating the NaBr solid in DMF. Then ~100 µl of IPABr solution was added into 1.5 ml of QD solution. After ~1 min of vortexing, the mixture was centrifuged at 7,800 r.p.m. for ~1 min to remove any insoluble solids. Then ~4 ml of methyl acetate was added to the mixture to precipitate the QDs. After centrifuging, the supernatant was discarded while the precipitate was resuspended into ~1 ml of toluene. Additional centrifugation (at 7,800 r.p.m.) was necessary if turbidity still existed in the supernatant. The exchange was repeated once or twice with 50 µl of IPABr solution. Additional methyl acetate was used to precipitate the QDs after each exchange cycle. NaBr DMF solution (20 µl) was used to perform one further ligand exchange. The exchanged QDs were suspended in 0.5 ml of octane/toluene with 50 µl of ethyl acetate to form QD ink. An additional small amount of DMF was in some cases used to resuspend QDs. The ink was centrifuged at 14,500 r.p.m. to remove any insoluble impurities before storage or use.

$CsPbBr_3$ QD solid film and LED fabrication. The concentration of the QD inks was determined by measuring their optical density (OD) at 400 nm. The molar concentration of particles was determined using the extinction coefficient reported elsewhere.[31] QD ink with a selected concentration (OD ≈ 0.15 for 4 nm QD ink and OD ≈ 0.9 for 7 nm QD ink, measured in a 1-mm-thick cuvette) was transferred into a glovebox. For QD solid films used in LEDs, indium tin oxide/glass substrates were cleaned ultrasonically with deionized water, acetone and 2-propanol for 30, 60 and 60 min, respectively. An aqueous solution of PEDOT:PSS (Clevios PVP AL 4083) was spin-coated onto the indium tin oxide/glass substrate at 6,000 r.p.m. for 30 s followed by baking at 150 °C for 30 min. After the substrate was cooled to room temperature, 5 mg ml^{-1} PTAA chlorobenzene solution was spin-coated onto the PEDOT:PSS layer and baked for 30 min at 170 °C. Next, a 10 mg ml^{-1} phenethylammonium bromide DMF solution was spin-coated onto the PTAA layer at 4,000 r.p.m. for 1 min. $CsPbBr_3$ ink was then spin-coated onto the PTAA at 2,000 r.p.m. for 1 min. Additionally, 10 µl of 2 mg ml^{-1} 1,3,5-tris(*N*-phenylbenzimiazole-2-yl) benzene (Lumtec) in methyl acetate was dropped onto the QD layer at 4,000 r.p.m.. The film was baked at 70 °C for 2 min. Next, using a thermal evaporation system, 60 nm of 1,3,5-tris(*N*-phenylbenzimiazole-2-yl) benzene, 1 nm of LiF and 150 nm of Al were deposited through shadow masks under a high vacuum (<10^{-4} Pa). The active area was fixed at 6.14 mm^2. All devices were encapsulated in UV-cured epoxy in a glovebox before characterization.

ζ-potential measurements. All electrophoretic mobility data were collected using a Zetasizer Nano-ZS system (Malvern Instruments). Colloidal QD solutions were put into quartz cuvettes with dip cell electrodes and then inserted into the instrument stage. All measurements include 100 scans and all measurements were repeated at least three times. QD colloids were diluted to concentrations that gave the best signal-to-noise ratio. The ζ potentials were obtained by using Henry's equation and the Hückel approximation for non-polar systems[48]:

$$\frac{U}{E} = \frac{2\varepsilon\zeta F(\kappa a)}{3\eta} \quad (2)$$

where U/E is the electrophoretic mobility obtained using the instrument, ζ is the ζ potential, ε is the solvent dielectric permittivity, η is the viscosity and $F(\kappa a)$ is the dimensionless Henry function. For non-polar systems, the Hückel approximation is applied and the value of Henry's function is close to 1. The mobility data for ζ-potential measurements in Fig. 1 are listed in Supplementary Table 1.

Absorption, photoluminescence, photoluminescence lifetime and PLQY measurements. Absorption spectra for QDs were collected using a fibre-coupled modular spectrometer (USB 2000+, Ocean Optics). Photoluminescence spectra of QD colloids and QD solid films were collected using a Horiba Fluorolog system with a xenon lamp as the excitation source. For both films and solutions, the sample was placed at an incidence angle of 30°. The photoluminescence spectra were collected using a calibrated monochromator/single-photon-detector assembly. The photoluminescence lifetime data were recorded using a time-correlated single-photon counting (TCSPC) system (Horiba). PLQY was measured using an integrating sphere and calculated according to a previously reported method[32].

Transient absorption measurements. Transient absorption spectra were recorded using a femtosecond pump–probe spectroscopy setup. The femtosecond laser pulses were produced by a regeneratively amplified Yb:potassium–gadolinium tungstate laser (Light Conversion, Pharos) at 1 kHz repetition rate. The fundamental beam was split into two beams, with one passing through an optical parametric amplifier (Light Conversion Orpheus) to generate a pump pulse at 400 nm, and was chopped. The other portion of the beam was directed onto a CaF crystal after focusing to generate white-light supercontinuum as the probe light. The power of the pump light was monitored using a power meter (Ophir) to keep the excitation fluence lower than the Auger threshold. The time delay was adjusted using a translation stage, optically delaying the probe pulses. The probe light intensity was measured with a charge-coupled device detector. QD solid sample was translated at a speed of 1 mm s^{-1} during measurements. Transient absorption bleach recovery dynamics were recorded at the band edge bleach peak position. The curve was fitted with a multiexponential decay function.

X-ray scattering measurements. Powder X-ray diffraction patterns were obtained using a Rigaku Miniflex 600 6G benchtop powder X-ray diffractometer with a Cu Kα radiation source. The QD powder samples were prepared by vacuum drying ~0.2 ml of QD solution with a concentration of ~40 mg ml^{-1} on a glass substrate.

GISAXS was conducted at the Hard X-ray MicroAnalysis beamline of the Canadian Light Source. An energy of 17.998 keV (λ = 0.6888 Å) was selected using a Si(111) monochromator. Patterns were collected on a SX165 charge-coupled device camera (Rayonix) placed at a distance of 175 mm from the sample. A lead beamstop blocked the direct beam. Images were calibrated using LaB_6 and processed with the Nika Igor plug-in (version 1.79)[33] and the GIXSGUI MATLAB plug-in (version 1.7.1)[34].

Electron microscopy measurements. Samples for TEM and scanning electron microscopy (SEM) imaging were prepared by spin-coating QD inks onto a copper TEM grid. TEM images were taken on a Hitachi HF-3300 instrument with a 300 kV acceleration voltage. SEM images were taken on a Hitachi SU3500 instrument. High-resolution scanning transmission electron microscopy (STEM) images were acquired on a double Cs-corrected ThermoFisher Titan Themis microscope operated at 300 kV. The images were acquired at a low dose and employed the drift-corrected frame integration method.

XPS measurements. XPS measurements were performed using a PHI5500 multitechnique system with a base pressure of ~10^{-9} torr. The X-ray radiation is Al Kα emission (1,486.7 eV; take-off angle, 75°).

FTIR, TGA and NMR measurements. FTIR spectra were collected using a Thermo Scientific Nicolet iS50 attenuated total reflectance FTIR system. Spectra were obtained using 16 scans with a resolution of 4 cm^{-1}. All QD solid film samples were cast on glass substrates. TGA experiments were conducted using a PerkinElmer Pyris 1 TGA instrument. Samples were prepared by drying 10–15 mg of QDs on a platinum sample pan. The solvent was evaporated by keeping the pan on a hotplate for 10 min. TGA involved an equilibration step 50 °C for 15 min, followed by heating to 750 °C at a heating rate of 10 °C min^{-1} under nitrogen. One-dimensional and 2D NOESY ^{1}H NMR spectra were collected using a 500 MHz Agilent DD2 NMR spectrometer. The QD samples for NMR measurements were suspended in benzene-d_6.

Exciton diffusion length measurements. Exciton diffusion length was estimated by acquiring transient absorption spectra following a previously reported method[35]. The exciton generated in $CsPbBr_3$ QD was transferred to smaller bandgap PbS QDs embedded in the $CsPbBr_3$ QD solid. By monitoring the band-edge carrier population using transient absorption spectra, we estimated the charge transfer time. In brief, a selected concentration of PbS QDs (~4 nm) was added to the $CsPbBr_3$ QD solution. When PbS QDs were homogeneously dispersed in the $CsPbBr_3$ QD solid, the inter-PbS QD distance L is the average centre-to-centre spacing between the two closest PbS QDs. The exciton diffusion length was

limited by the inter-QD distance. To determine the inter-PbS QD distance, the molar concentration of two kinds of QDs was determined via optical absorption. Knowing the absorption cross-section of each kind of QDs[31,36], we calculated the concentration of QDs (C_{PbS} and C_p). By controlling the volume of PbS QD solution added to $CsPbBr_3$ QD solution (V_{PbS} for PbS QD and V_p for $CsPbBr_3$), we obtained the molar ratio (X) of PbS QDs to $CsPbBr_3$ QDs from the equation:

$$X = \frac{C_{PbS} \times V_{PbS}}{C_p \times V_p} \quad (3)$$

The PbS QDs were embedded in the $CsPbBr_3$ QD superlattice, and the interdot distance was determined as:

$$L = d_{PbS} + d_p \times \sqrt[3]{\frac{1}{X}} \quad (4)$$

where d is the diameter of the QD.

LED performance and operating stability measurements. The current density–luminance–voltage characteristics of the QD LEDs were obtained under ambient conditions using a Keithley 647 source meter. The electroluminescence spectra were collected using a calibrated fibre-coupled spectrometer (USB 4000, Ocean Optics). The luminance values were cross-checked using a luminance meter (Monica LS-110). The operational stability was obtained in constant current mode using a source meter. The electroluminescence intensity was monitored using a photodetector.

For LED characterization under pulsed mode, a silicon photodiode (PDA36A, Thorlabs) was used to collect photons emitted from the device. A square-wave electric pulse with various duty cycles was generated using a function generator (3350B, Agilent). The waveform of the pluses and the photodiode signal were monitored using an oscilloscope (DSO1002A, Agilent). Device performance for pulsed studies was also cross-checked using continuous-wave mode.

Perovskite QD solid film characterizations. The current–voltage curves of electron-/hole-only devices for SCLC measurements were obtained with a computer-controlled Keithley 2400 source meter. The film thickness was determined with a Hitachi SU3500 instrument. The photocurrent of the photoresistor was obtained with Agilent-Keysight 4156A sweep generators. To excite the photoresistor with photons with energy above the bandgap, a 405 nm diode laser was used. The laser light was attenuated by a series of neutral density filters for various excitation powers. The excitation densities were calculated via cross-section data available from other reports[31]. For sub-bandgap excitations, a femtosecond fundamental beam was sent through an optical parametric amplifier to generate laser pulses of variable wavelengths. The laser beam was collimated before being sent to the device.

Data availability

The authors declare that the main data supporting the findings of this study are available within the letter and its Supplementary Information. Extra data are available from the corresponding authors upon reasonable request.

References

31. Maes, J. et al. Light absorption coefficient of $CsPbBr_3$ perovskite nanocrystals. *J. Phys. Chem. Lett.* **9**, 3093–3097 (2018).
32. de Mello, J. C., Wittmann, H. F. & Friend, R. H. An improved experimental determination of external photoluminescence quantum efficiency. *Adv. Mater.* **9**, 230–232 (1997).
33. Ilavsky, J. Nika: software for two-dimensional data reduction. *J. Appl. Crystallogr.* **45**, 324–328 (2012).
34. Jiang, Z. GIXSGUI: a MATLAB toolbox for grazing-incidence X-ray scattering data visualization and reduction, and indexing of buried three-dimensional periodic nanostructured films. *J. Appl. Crystallogr.* **48**, 917–926 (2015).
35. Proppe, A. H. et al. Picosecond charge transfer and long carrier diffusion lengths in colloidal quantum dot solids. *Nano Lett.* **18**, 7052–7059 (2018).
36. Cademartiri, L. et al. Size-dependent extinction coefficients of PbS quantum dots. *J. Am. Chem. Soc.* **128**, 10337–10346 (2006).

Acknowledgements

This work was supported by the Ontario Research Fund–Research Excellence Program and the Natural Sciences and Engineering Research Council of Canada (NSERC, grant number 537463-18). M.I.S. acknowledges the support of the Banting Postdoctoral Fellowship Program, administered by the Government of Canada. We acknowledge financial support from the Natural Science Foundation of China (numbers 51821002 and 91733301) and the Collaborative Innovation Centre of Suzhou Nano Science and Technology. Y.-K.W. also acknowledges the financial support of the China Scholarship Council (number 201806920067). We thank Huawei Canada for their financial support. Z.-H.L. and all co-authors from the Department of Materials Science and Engineering at the University of Toronto acknowledge the financial support from the Natural Sciences and Engineering Research Council of Canada (NSERC, grant number 216956-12) and the National Natural Science Foundation of China (grant number 11774304).

Author contributions

Y.D., Y.-K.W. and F.Y. conceived the study. Y.D. and Y.-K.W. synthesized the $CsPbBr_3$ perovskite QDs and developed the ligand exchange method. Y.D. performed steady-state absorption and photoluminescence spectra measurements, time-correlated single-photon counting measurements and transient absorption spectroscopy measurements. Y.-K.W. and F.Y. fabricated the LED devices, performed XRD measurements and characterized the LEDs. B.C., S.-W.B. and M.W. performed TEM, SEM and STEM imaging. J.F. performed FTIR spectroscopy measurements. L.K.S. performed the TGA. M.-J.C. and M.C. performed the ζ-potential measurements. F.Y., P.L. and H.T.K. performed XPS measurements. R.Q.-B. and A.J. performed GISAXS measurements. Y.H., Y.L., B.S., S.L., D.M., P.T., F.D., H.E., E.K. and S.H. contributed to device fabrication and data analyses. Y.D. and O.V. performed the device simulation. M.I.S., Z.-H.L and E.H.S. supervised the project. All authors discussed the results and commented on the manuscript.

Competing interests

The authors declare no competing interests.

Additional information

Supplementary information is available for this paper at https://doi.org/10.1038/s41565-020-0714-5.

Correspondence and requests for materials should be addressed to Z.H.L. or E.H.S.

Reprints and permissions information is available at www.nature.com/reprints.